

Supplementary Information for “Non-Fermi liquid to charge-transfer Mott insulator in flat bands of copper-doped lead apatite”

Sun-Woo Kim,^{1,*} Kristjan Haule,² Gheorghe Lucian Pascut,^{3,†} and Bartomeu
Monserrat^{1,4,‡}

¹*Department of Materials Science and Metallurgy, University of Cambridge, 27 Charles
Babbage Road, Cambridge CB3 0FS, United Kingdom*

²*Center for Materials Theory, Department of Physics & Astronomy, Rutgers University,
Piscataway, NJ 08854, USA*

³*MANSiD Research Center and Faculty of Forestry, Stefan Cel Mare University (USV),
Suceava 720229, Romania*

⁴*Cavendish Laboratory, University of Cambridge, J. J. Thomson Avenue, Cambridge CB3
0HE, United Kingdom*

Contents

Supplementary Note 1. Comparison of calculated $P3$ structure with experimental data	2
Supplementary Note 2. Comparison of electronic structures between DFT and eDMFT	3
2.1. Metallic states	3
2.2. Insulating states	4
Supplementary Note 3. Temperature dependence of the density of states	6
Supplementary Note 4. First Matsubara frequency rule	7
Supplementary Note 5. Details on the self energy	9
5.1. U and J dependence	9
5.2. Non-correlated orbitals	11
Supplementary References	12

Supplementary Note 1. COMPARISON OF CALCULATED $P3$ STRUCTURE WITH EXPERIMENTAL DATA

In this section, we present a detailed comparison between our calculated $P3$ structure and experimental data. The calculated lattice parameters are in remarkable agreement with the experimental data (Table S1).

TABLE S1: Comparison of lattice parameters of $\text{Pb}_9\text{Cu}(\text{PO}_4)_6\text{O}$ between theory and experiment.

Reference	a (Å)	c (Å)	Volume (Å ³)
This work (DFT-PBE)	9.847	7.375	619.29
Expt. [1] (powder sample)	9.843	7.428	623.24
Expt. [2] (powder sample)	9.853	7.442	625.69
Expt. [2] (powder sample)	9.848	7.438	624.72
Expt. [2] (single crystal sample)	9.838	7.422	622.11
Expt. [2] (single crystal sample)	9.814	7.437	620.33
Expt. [2] (single crystal sample)	9.778	7.397	612.47
Expt. [2] (single crystal sample)	9.798	7.398	615.06

Additionally, we simulate X-ray diffraction pattern for the $P3$ structure, which also shows excellent agreement with the experimental results (Fig. S1).

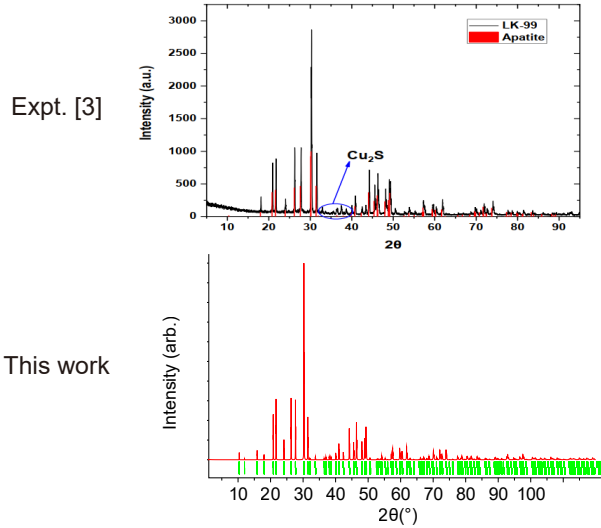


FIG. S1: Comparison of XRD patterns between theory and experiment. The experimental data figure is taken from Ref. [3].

Supplementary Note 2. COMPARISON OF ELECTRONIC STRUCTURES BETWEEN DFT AND EDMFT

2.1. Metallic states

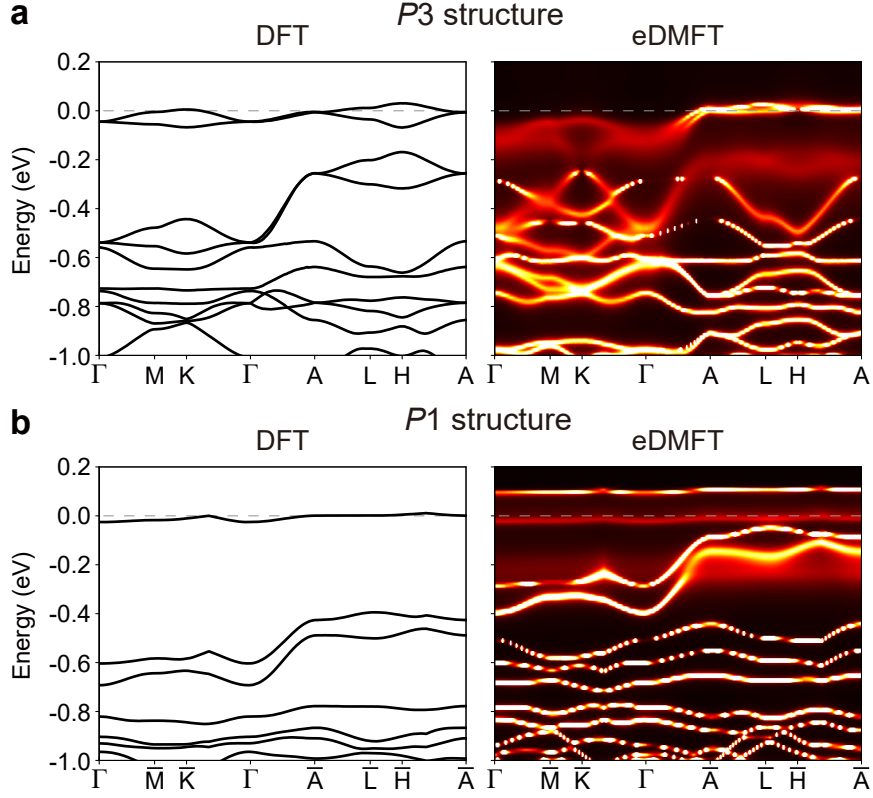


FIG. S2: **Comparison of metallic electronic structures obtained using DFT and eDMFT calculations.** **a,b** Nonmagnetic DFT band structure and paramagnetic eDMFT spectral function for **a** the $P3$ structure and **b** the $P1$ structure. For the DFT calculations, the PBE exchange-correlation functional is used and a nonmagnetic state is imposed. For the eDMFT calculations, $U = 3$ eV and $J = 1$ eV are used at a temperature of 300 K for the paramagnetic state.

Figure S2 compares the DFT and eDMFT electronic structures for metallic states. For the $P3$ structure, both methods show two flat bands near the Fermi level (Fig. S2a). However, there are notable differences between the eDMFT spectral function and the single-particle DFT band structure. Specifically, the spectral function exhibits incoherent states near the Fermi level, characterized by broadened spectral weight due to electron correlations. This broadening causes certain coherent band states to appear below the Fermi level in eDMFT, which do not exist in the corresponding energy range of the DFT band structure. Additionally, eDMFT shows changes in other coherent bands with an overall bandwidth

renormalization.

For the $P1$ structure, eDMFT reduces the energy gap between the single flat band and its closest lower band, leading to the formation of highly incoherent states at the Fermi level across the entire Brillouin zone (Fig. S2b). These incoherent states exhibit a pseudo-gap-like density of states, which cannot be captured by DFT due to their highly correlated nature, as discussed in the main text.

As a note of clarification, we only obtain a metallic DFT band structure by imposing a non-magnetic state. The ground state corresponding to our DFT calculation is a ferromagnetic insulator (see next section). Additionally, we note that depending on the choice of U in a DFT+ U context, we could also get a ferromagnetic metal as the ground state.

2.2. Insulating states

Figure S3 compares the DFT and eDMFT electronic structures for insulating states. To obtain insulating states, we introduce a ferromagnetic ordering for the DFT calculations. With our chosen Hubbard parameter of $U = 3$ eV, DFT yields Cu magnetic moments along the z axis of 0.712 and $0.671 \mu_B$ per unit cell for the $P3$ and $P1$ structures, respectively. Both methods appear to show overall agreement for both the $P3$ and $P1$ structures when only comparing the band dispersions. However, a key difference between the two methods appears when considering the spin character: in DFT, both structures show a single spin-polarized unoccupied narrow flat band and spin-polarized occupied bands, leading to an overall ferromagnetic insulating state. By contrast, eDMFT shows non-spin-polarized paramagnetic unoccupied and occupied bands.

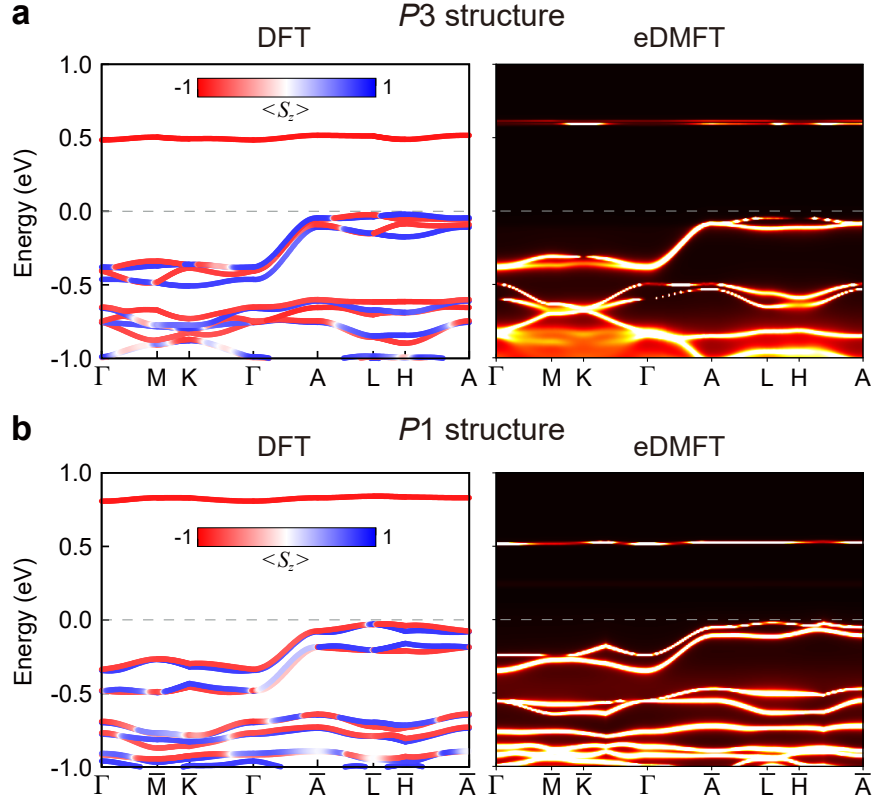


FIG. S3: Comparison of insulating electronic structures obtained using DFT and eDMFT calculations. **a,b** Ferromagnetic DFT band structure and paramagnetic eDMFT spectral function for **a** the $P3$ structure and **b** the $P1$ structure. For the DFT calculations, the PBEsol [4] exchange-correlation functional with Hubbard $U = 3$ eV and spin-orbit coupling is used for the ferromagnetic state, utilizing the VASP code [5, 6]. The spin-polarized DFT band structures are projected onto the spin S_z component. For eDMFT calculations, $U = 7$ eV and $J = 1$ eV are used at a temperature of 300 K for the paramagnetic state.

Supplementary Note 3. TEMPERATURE DEPENDENCE OF THE DENSITY OF STATES

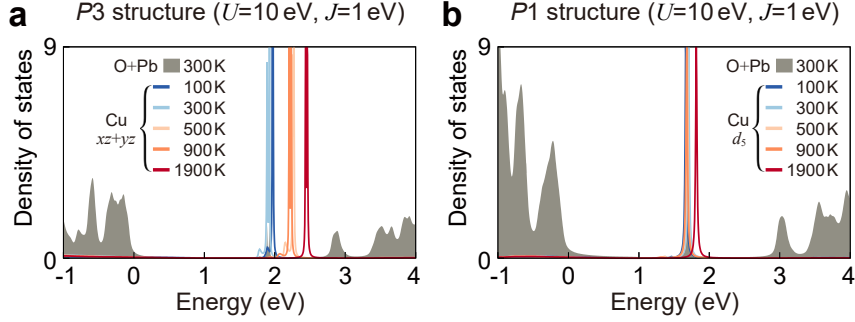


FIG. S4: **Temperature dependence of the density of states (DOS) for insulating states.** **a,b** DOS of correlated copper d orbitals for the **a** $P3$ structure and **b** $P1$ structure as a function of temperature. $U = 10$ eV and $J = 1$ eV are used. For comparison, the DOS of oxygen and lead states are shown in shaded grey.

In the main text, we discuss the formation of a narrow unoccupied flat band within the fundamental bulk gap as the $P3$ or $P1$ structures undergo a metal-insulator transition with increasing U and/or decreasing J . We demonstrate that this narrow unoccupied band in the insulating states remains positioned within the fundamental bulk gap despite wide temperature variations ranging from 100 K to 1900 K for both structures (Fig. S4). As temperature increases, the narrow unoccupied band blueshifts towards the conduction bulk states, with a larger shift in the $P3$ structure compared to the $P1$ structure.

Supplementary Note 4. FIRST MATSUBARA FREQUENCY RULE

In a Fermi liquid, the imaginary part of the self energy at the first Matsubara frequency, $\text{Im } \Sigma(i\omega_0)$, exhibits a T -linear scaling behaviour at low temperatures, which is referred to as the first Matsubara frequency rule [7]. This linear dependence arises because the self energy of a Fermi liquid at low temperatures and frequencies takes the following form on the real axis:

$$\text{Re } \Sigma(\omega) = (1 - Z^{-1})\omega, \quad \text{Im } \Sigma(\omega, T) = -C(\omega^2 + \pi^2 T^2), \quad (1)$$

where Z is the quasiparticle renormalization factor and C is a coefficient. Under analytical continuation to Matsubara frequencies $i\omega_n$, the imaginary part of the self energy becomes

$$\text{Im } \Sigma(i\omega_n, T) = (1 - Z^{-1})\omega_n + C(\omega_n^2 - \pi^2 T^2). \quad (2)$$

At the first Matsubara frequency $\omega_0 = \pi T$, the quadratic temperature term vanishes and we obtain:

$$\text{Im } \Sigma(i\omega_0, T) = (1 - Z^{-1})\pi T, \quad (3)$$

leaving only the linear temperature term.

Figure S5 shows the imaginary part of the self energy at the first Matsubara frequency, $\text{Im } \Sigma(i\omega_0)$, for metallic states in the $P3$ and $P1$ structures. For both structures, the values of $\text{Im } \Sigma(i\omega_0)$ for non-correlated orbitals (black) exhibit perfect linear- T scaling behaviour even at higher temperatures, consistent with their Fermi liquid nature. In contrast, the values of $\text{Im } \Sigma(i\omega_0)$ for correlated orbitals for both structures (red), which are relevant for states near the Fermi level, deviate significantly from linearity, violating the first Matsubara frequency rule. This confirms the non-Fermi-liquid nature of the metallic states in both structures.

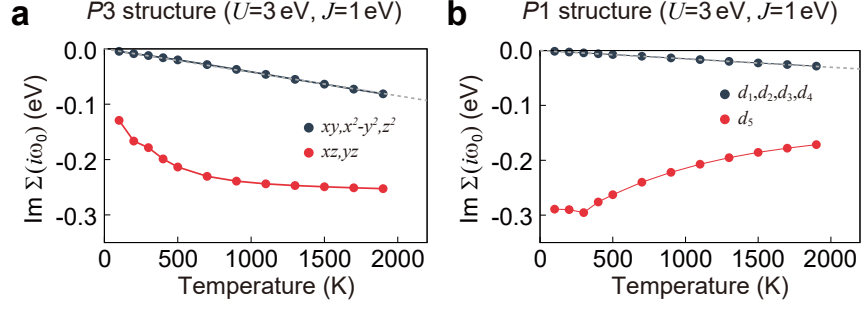


FIG. S5: **First Matsubara frequency rule.** **a,b** The imaginary part of the self energy at the first Matsubara frequency, $\text{Im}\Sigma(i\omega_0)$, for the non-Fermi-liquid states in **a** the $P3$ structure and **b** the $P1$ structure. Red lines and symbols denote the average $\text{Im}\Sigma(i\omega_0)$ for correlated orbitals, while black lines and symbols represent the corresponding average for non-correlated orbitals. Grey dotted lines indicate linear fits of $\text{Im}\Sigma(i\omega_0)$ in the low-temperature regions for the non-correlated orbitals. The values of $\text{Im}\Sigma(i\omega_0)$ for non-correlated orbitals exactly follow these linear fits even at higher temperatures, whereas the trends for correlated orbitals deviate significantly from linearity.

Supplementary Note 5. DETAILS ON THE SELF ENERGY

5.1. U and J dependence

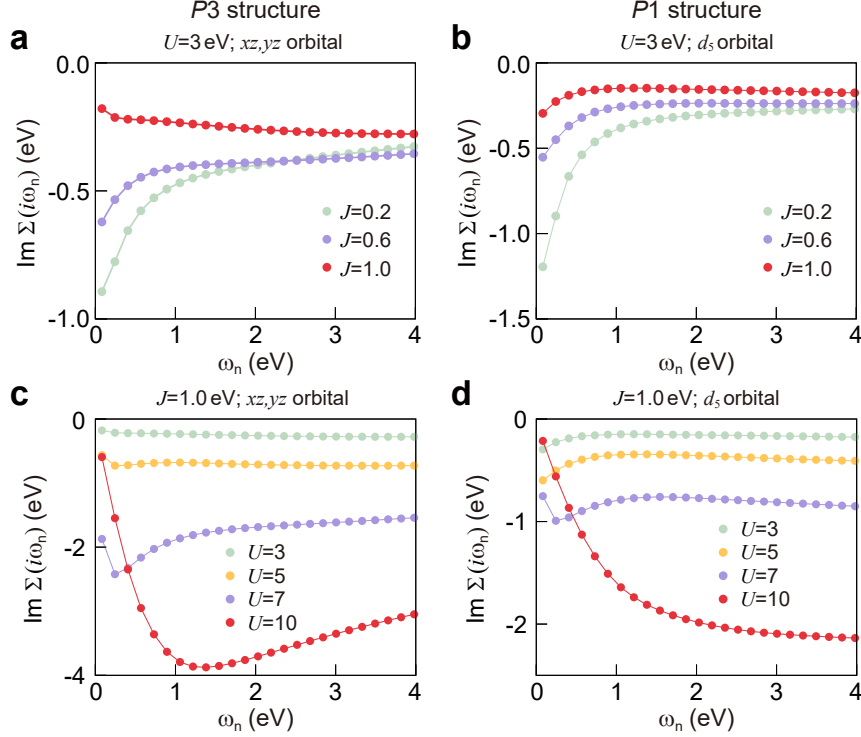


FIG. S6: **Influences of Hubbard U and Hund's coupling J on the self energy of correlated copper d orbital states.** **a,b** The imaginary part of the self energy on the imaginary axis, $\text{Im}\Sigma(i\omega_n)$, at fixed $U = 3$ eV as a function of J for **a** the $P3$ structure and **b** the $P1$ structure. **c,d** $\text{Im}\Sigma(i\omega_n)$ at fixed $J = 1$ eV as a function of U for **c** the $P3$ structure and **d** the $P1$ structure.

In the main text, we analyze the NFL states of both structures at $U = 3$ eV and $J = 1$ eV in detail, assigning the NFL state in the $P3$ structure as a bad-metallic NFL and the NFL state in the $P1$ structure as a pseudogap NFL based on their detailed low-frequency behaviour of $\text{Im}\Sigma(i\omega_n)$, their electronic structures, and the temperature dependence of their scattering rates. A crucial factor distinguishing these two NFL states is the slope A of $\text{Im}\Sigma(i\omega_n)$ at low frequencies: the bad-metallic NFL shows a negative slope $A < 0$, whereas the pseudogap NFL shows a positive slope $A > 0$.

To gain further insights into these NFL states, we investigate $\text{Im}\Sigma(i\omega_n)$ by varying J values at fixed $U = 3$ eV. As J decreases, the magnitude of $\text{Im}\Sigma(i\omega_n)$ increases for both structures, reflecting enhanced electron correlations due to the increased effective U (Figs. S6a,b). Notably, in the $P3$ structure, the slope A changes sign as J decreases, indicating a tran-

sition to a pseudogap NFL state. For $J \leq 0.6$ eV, the behaviour of $\text{Im} \Sigma(i\omega_n)$ in the $P3$ structure becomes similar to that in the $P1$ structure, suggesting that the pseudogap NFL state represents a more correlated NFL state. This implies that the two entangled energy bands in the $P3$ structure result in a metallic state with reduced correlations at identical U and J values.

We also examine the evolution of $\text{Im} \Sigma(i\omega_n)$ during the metal-insulator transition by increasing U at fixed $J = 1$ eV (Figs. S6c,d). As U increases, the magnitude of $\text{Im} \Sigma(i\omega_n)$ increases, leading to a transition from metallic states to insulating states for both structures. As discussed in detail in the main text, at $J = 1$ eV, both structures are metallic NFL states at $U = 3$ and 5 eV, and become charge-transfer Mott insulating states at larger U . For the $P3$ structure, the metallic states maintain their bad-metallic NFL characteristics with increasing U , since the slope remains the same even as it becomes an insulator. For the $P1$ structure, the metallic states also maintain their NFL characteristics with increasing U , but the slope changes sign upon becoming an insulator. In the insulating states, both structures exhibit low-frequency values of $\text{Im} \Sigma(i\omega_n)$ approaching zero at zero imaginary frequency, as there are no electrons to scatter.

5.2. Non-correlated orbitals

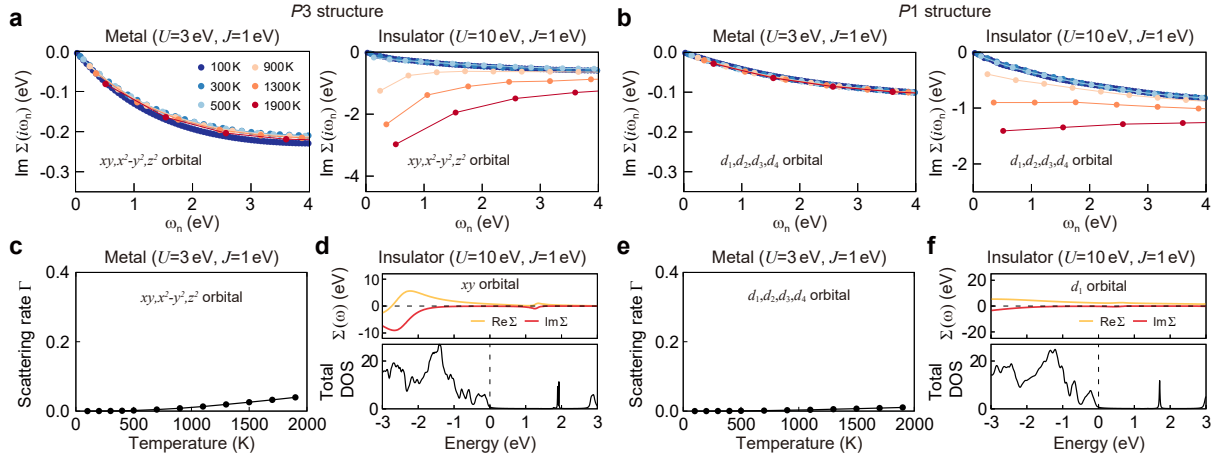


FIG. S7: **Self energy and scattering rate of non-correlated orbitals.** **a,b** Temperature evolution of the imaginary part of the self energy on the imaginary axis, $\text{Im}\Sigma(i\omega_n)$, for **a** the $P3$ structure and **b** the $P1$ structure. We display $\text{Im}\Sigma(i\omega_n)$ for the non-correlated orbitals by averaging them (see Fig. 4 in the main text for the self-energy of correlated orbitals). **c** Scattering rate of non-correlated orbitals in the metallic state of the $P3$ structure as a function of temperature. The scattering rate is averaged over the d_{xy} , $d_{x^2-y^2}$, and d_{z^2} orbitals. **d** Self energy of the d_{xy} orbital on the real axis and total DOS of the insulating state of the $P3$ structure. **e** Scattering rate of non-correlated orbitals in the metallic state of the $P1$ structure as a function of temperature. The scattering rate is averaged over the d_1 , d_2 , d_3 , and d_4 orbitals. In **c,e**, the scattering rate $\Gamma \sim -\text{Im}\Sigma(i0^+)$ is obtained using a linear fit over the first two Matsubara frequencies. **f** Self energy of the d_1 orbital on the real axis and total DOS of the insulating state of the $P1$ structure.

For completeness, we also provide a detailed analysis on the self energy of the non-correlated orbitals in Fig. S7: d_{xy} , $d_{x^2-y^2}$, and d_{z^2} orbitals for the $P3$ structure, and d_1 , d_2 , d_3 , and d_4 orbitals for the $P1$ structure, which are away from the Fermi level. In the metallic states, these non-correlated orbitals are Fermi liquid states for both structures, as confirmed by the first Matsubara frequency rule in Supplementary Note 4. The low-frequency behaviour of $\text{Im}\Sigma(i\omega_n)$ for the non-correlated orbitals in metallic states shows linear behaviour and zero scattering rate at low temperatures (left panels in Figs. S7a,b). The scattering rates of the non-correlated orbitals for both structures exhibit quadratic temperature dependence (Figs. S7c,e), as expected for Fermi liquid states. In the insulating states for both structures, the real and imaginary parts of the self energy for the non-correlated orbitals on the real axis exhibit featureless values close to zero, without a pole structure within the gap (Figs. S7d,f). This confirms that the non-correlated orbitals are not relevant for Mott gap opening.

-
- [1] Lee, S. *et al.* Superconductor $\text{Pb}_{10-x}\text{Cu}_x(\text{PO}_4)_6\text{O}$ showing levitation at room temperature and atmospheric pressure and mechanism. *arXiv preprint arXiv:2307.12037* (2023).
- [2] Puphal, P. *et al.* Single crystal synthesis, structure, and magnetism of $\text{Pb}_{10-x}\text{Cu}_x(\text{PO}_4)_6\text{O}$. *APL Mater.* **11**, 101128 (2023).
- [3] Lee, S., Kim, J.-H. & Kwon, Y.-W. The first room-temperature ambient-pressure superconductor. *arXiv preprint arXiv:2307.12008* (2023).
- [4] Perdew, J. P. *et al.* Restoring the density-gradient expansion for exchange in solids and surfaces. *Phys. Rev. Lett.* **100**, 136406 (2008).
- [5] Kresse, G. & Furthmüller, J. Efficiency of ab-initio total energy calculations for metals and semiconductors using a plane-wave basis set. *Comput. Mater. Sci.* **6**, 15–50 (1996).
- [6] Kresse, G. & Furthmüller, J. Efficient iterative schemes for ab initio total-energy calculations using a plane-wave basis set. *Phys. Rev. B* **54**, 11169–11186 (1996).
- [7] Chubukov, A. V. & Maslov, D. L. First-Matsubara-frequency rule in a Fermi liquid. I. Fermionic self-energy. *Phys. Rev. B* **86**, 155136 (2012).